Similar spatial patterns of global climate response to aerosols from different regions

Matthew Kasoar, Dilshad Shawki, and Apostolos Voulgarakis

Supplementary Information:

Additional discussion: Tables S1 and S2

Explaining the variations in forcing per unit emission change

Removing SO_2 emissions from East Asia results in a much smaller forcing per unit emission than removing SO_2 emissions from North America or Europe (Table S1). To explain this, we note that East Asia has much higher emissions of all aerosol species, not just sulfate. As a result, the total aerosol loading above East Asia after SO_2 emissions are removed is considerably higher than that over North America or Europe, where the total aerosol burden becomes very small once regional SO_2 emissions are removed. Aerosol indirect effects saturate at higher particle number concentrations[1,2], implying that the cloud albedo sensitivity to a change in sulfate burden would presumably be greater over North America and Europe. This provides one reason why the all-sky forcing due to removing SO_2 emissions from North America or Europe might be greater than that for East Asia, even though the clear-sky forcing is smaller (Table S2). Additionally, in these simulations it is climatologically cloudier over East Asia in general (not shown), and this would also help to mask the direct radiative effect of sulfate in cloudy-sky conditions. From these data it is hard to determine which of these effects, if either, is the dominant factor, though it could be tested in future work with additional simulations (e.g. turning off indirect effects (to test the importance of cloud masking only), or removing all other aerosol species except sulfate (to test the importance of the cloud albedo effect saturating in high background aerosol conditions)).

Variations in the efficacy of regional forcings

The global temperature response per unit forcing in Table S1 is around 30% larger for a forcing over North America than over either Europe or East Asia, which both have very similar values. This suggests a possible additional source of regional diversity – as well as a given emissions change resulting in a stronger or weaker radiative forcing depending on the region of emission, the efficacy

of a given forcing – its relative effectiveness at producing a global temperature response – might also vary depending on the region over which the forcing is located. We note, however, that the global mean ERFs and surface temperature responses in the North America and Europe perturbations are within the $2\sigma_c$ internal variability range (see Methods) of each other, and consequently this difference between the climate sensitivities, though relatively large at ~30%, is not statistically significant. Robust conclusions are therefore confounded by the relatively small values of both the numerator and denominator, compared with experiments such as 2 × or 4 × CO_2 perturbations which are more typically employed to calculate climate sensitivities in global models. Tentatively, however, it seems that the climate sensitivity to the North America perturbation (1.0 K (W m^{-2})$^{-1}$) is similar to that found for a global 2 × CO2 perturbation in this model[3] of 1.1 K (W m^{-2})$^{-1}$, whereas the sensitivity in the other regional aerosol perturbations is somewhat lower (0.6-0.7 K (W m^{-2})$^{-1}$), suggesting that in general the global sensitivity to a unit of regional forcing may be lower than the sensitivity to a unit of global forcing, except perhaps in the North American case. Shindell (2014)[4] found that in transient simulations driven by historical forcing, the global sensitivity to aerosols was in fact greater than to CO_2 forcing in CMIP5 models, however this is attributed to faster land responses in the northern hemisphere, and so the transient nature of the experiments was critical to that result.

Additional discussion: Table S4 and Figures S4-S6

Analysis of the leading surface temperature EOF

The three leading modes for global surface temperature and 500hPa geopotential height between them explain 35-40% of the total variability in the simulated climate system, with the leading two modes explaining very similar fractions of the variance in these two fields (Table S4). The first modes explain just over 20%, and the second just over 10%, of the variances for both surface temperature and 500hPa geopotential height. As a result of performing the EOF calculation globally,

an ENSO-like pattern in the tropical Pacific is seen to be convolved with all the leading surface temperature EOFs (Figure 4a and S4a,b), rather than appearing as a single mode of variability itself. Aside from this, the leading temperature EOF is characterised by a largely uniform global pattern of the same sign almost everywhere (Figure S4a). Inspection of the corresponding principle component timeseries for this mode (Figure S5) reveals that rather than oscillating, this mode increases steadily from a negative phase to a positive phase over the course of the simulation, and we therefore interpret this as corresponding to a known drift in global temperature of the control climate over the 200 years (Figure S6). It is not surprising that this drift would be the dominant 'variability' over the 200 year course of the simulation, and so this first EOF is probably not particularly revealing, and is not truly an intrinsic mode of variability.

References

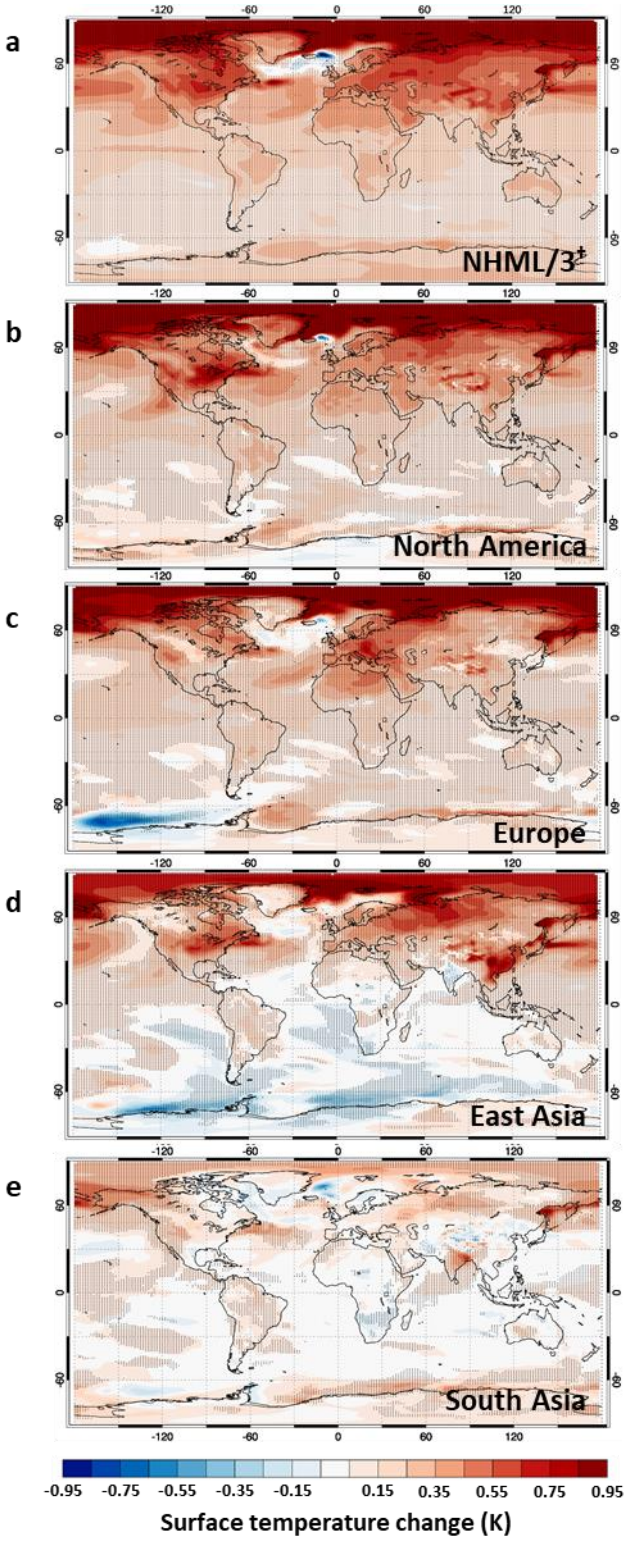
1 Carslaw, K. S. *et al.* Large contribution of natural aerosols to uncertainty in indirect forcing. *Nature* **503**, 67-71, doi:10.1038/nature12674 (2013).

2 Wilcox, L. J., Highwood, E. J., Booth, B. B. B. & Carslaw, K. S. Quantifying sources of inter-model diversity in the cloud albedo effect. *Geophysical Research Letters* **42**, 1568-1575, doi:10.1002/2015gl063301 (2015).

3 Samset, B. H. *et al.* Fast and slow precipitation responses to individual climate forcers: A PDRMIP multimodel study. *Geophysical Research Letters* **43**, 2782-2791, doi:10.1002/2016gl068064 (2016).

4 Shindell, D. T. Inhomogeneous forcing and transient climate sensitivity. *Nature Climate Change* **4**, 274-277, doi:10.1038/nclimate2136 (2014).

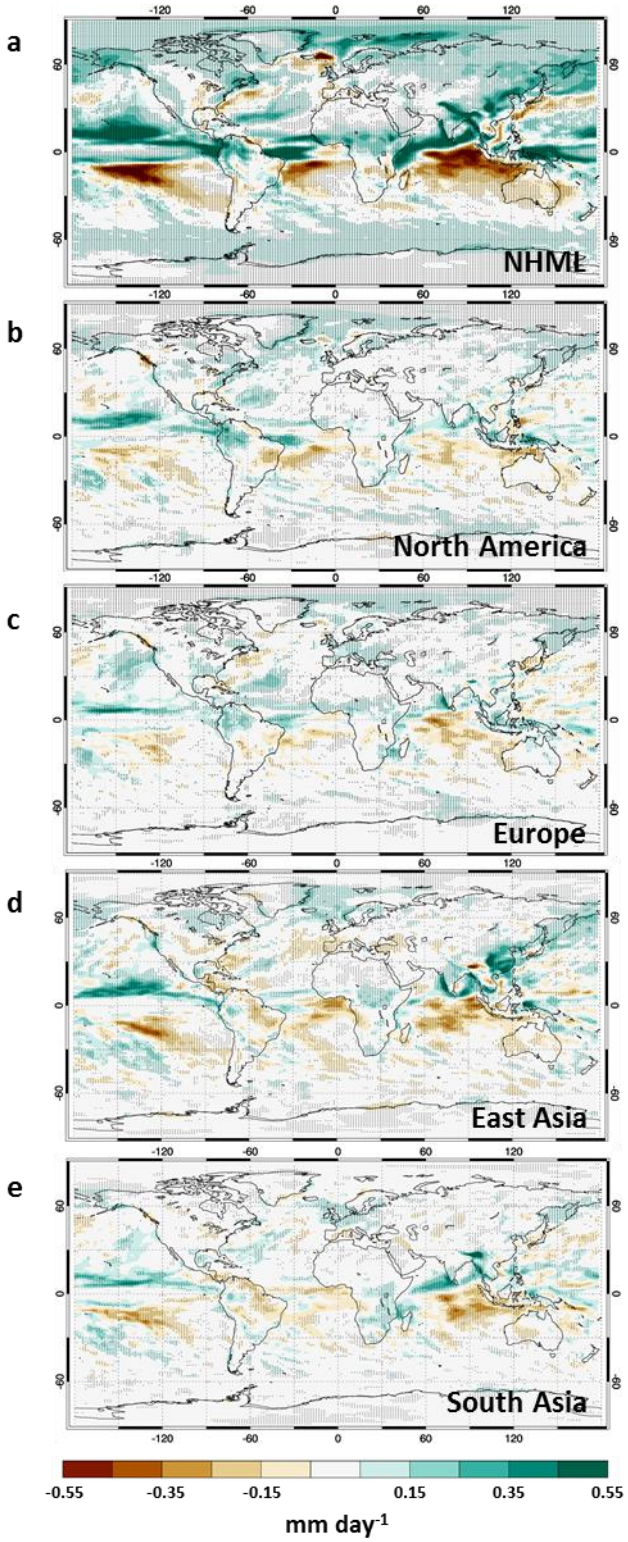
5 Myhre, G. *et al.* PDRMIP: A Precipitation Driver and Response Model Intercomparison Project—Protocol and Preliminary Results. *Bulletin of the American Meteorological Society* **98**, 1185-1198, doi:10.1175/bams-d-16-0019.1 (2017).



84

85 **Figure S1 | Surface temperature changes due to removing SO_2 emissions from a) the northern**
86 **hemisphere mid-latitudes (NHML), b) North America, c) Europe, d) East Asia, and e) South**
87 **Asia.** Responses are diagnosed from 150-year annual averages of coupled simulations. Stippling
88 indicates that the change at that grid-point exceeded two standard deviations of the 150-year mean

surface temperature in six different control simulations, as described in the Methods section of the main manuscript. † Note that the NHML changes have been divided by 3 in order to show them on the same contour scale.



93

94 **Figure S2 | Precipitation changes due to removing SO_2 emissions from a) the northern**
95 **hemisphere mid-latitudes (NHML), b) North America, c) Europe, d) East Asia, and e) South**
96 **Asia.** Responses are diagnosed from 150-year annual averages of coupled simulations. Stippling
97 indicates that the change at that grid-point exceeded two standard deviations of the 150-year mean

precipitation in six different control simulations, as described in the Methods section of the main manuscript.

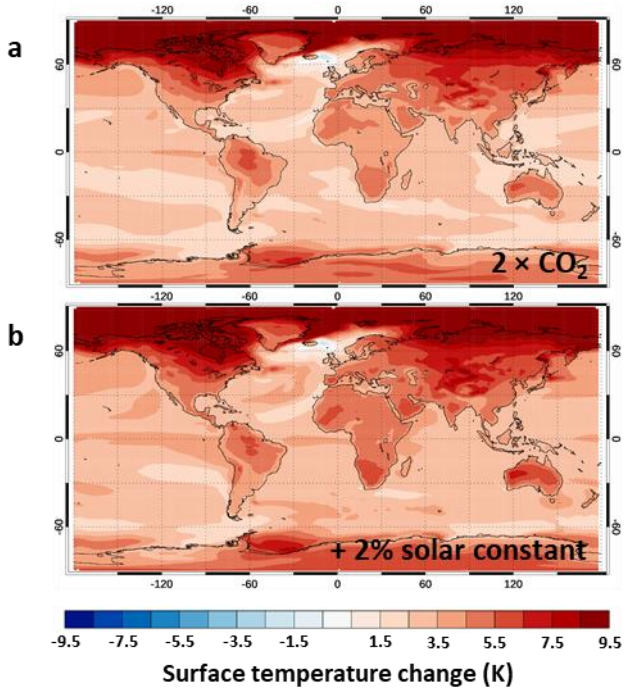
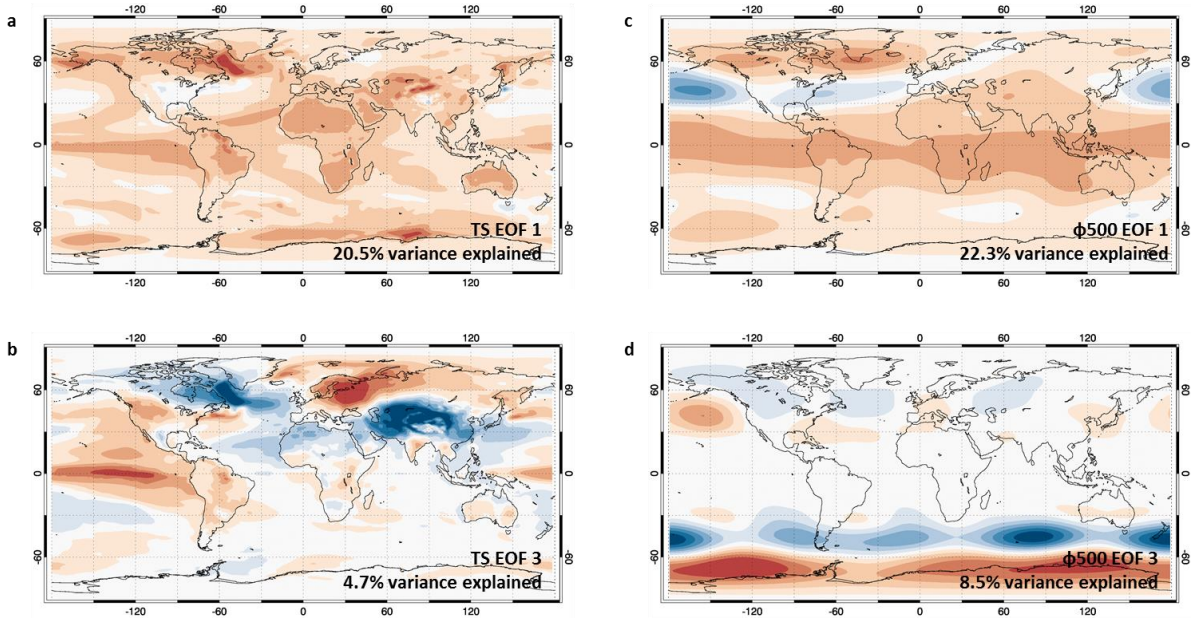


Figure S3 | Surface temperature changes due to a) doubling CO_2 atmospheric concentration, and b) increasing the solar constant by 2%. Responses are diagnosed from 50-year annual averages of the HadGEM3-GA4 coupled simulations performed for the PDRMIP project, as described in[3,5]. These simulations used a near-identical model configuration as the present study, except that aerosol concentrations were prescribed and non-interactive.



114

115 **Figure S4 | First and third EOFs of global annual mean surface temperature (a, b), and 500 hPa**
116 **geopotential height (ϕ500, c, d) in the control simulation.** The sign and absolute magnitude of
117 the EOF patterns are arbitrary, so we show them here without a scale range.

118

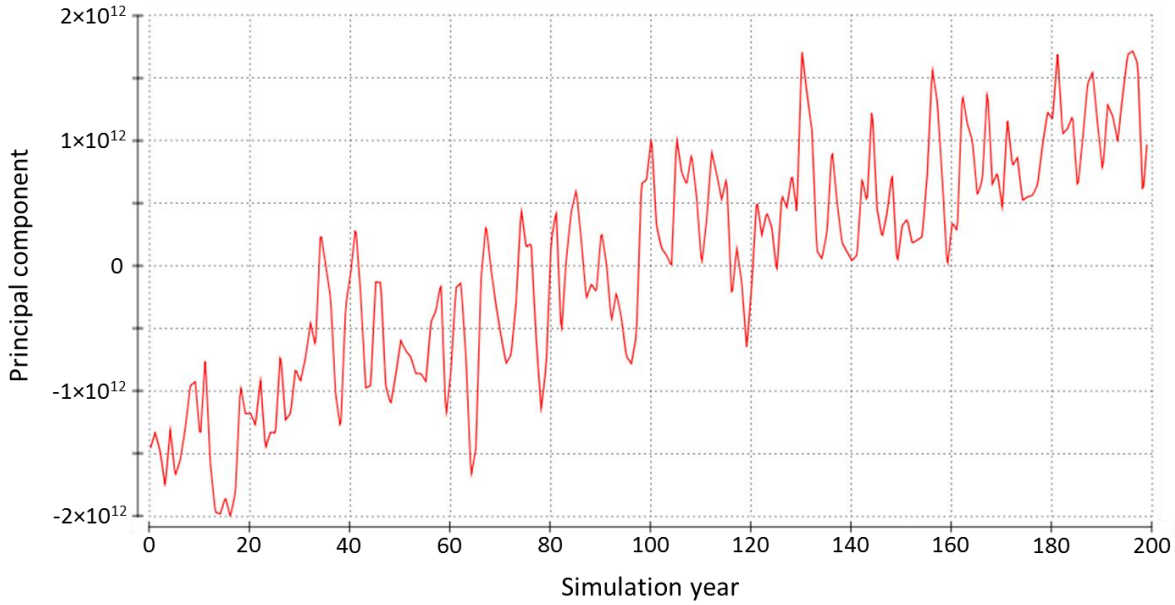


Figure S5 | Principal component timeseries for the leading EOF of annual mean surface temperature in the control simulation.

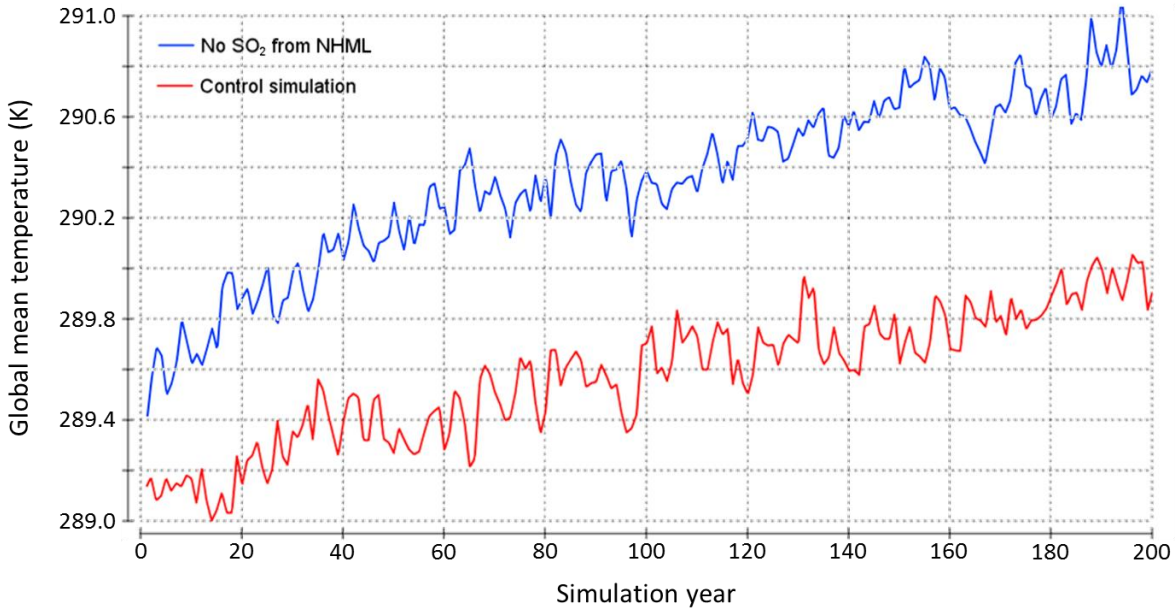


Figure S6 | Timeseries of global annual mean temperature in the control simulation (red line) and, for comparison, the simulation with no SO_2 emissions from the northern hemisphere mid-latitudes (NHML). The control simulation displays a drift in global mean temperature over the course

of the 200 years which is also present in the perturbation simulations. However, the comparison shows that after adjusting over a relatively short timescale, the NHML perturbation simulation drifts approximately in parallel with the control simulation. We therefore believe that by taking averages over the last 150 years of each simulation, the difference between perturbation and control simulations represents the response to the emission perturbation and the effect of the drift is effectively subtracted off.

Table S1 | Change in global mean surface temperature in HadGEM3-GA4 per unit emission and per unit forcing. Left column shows the surface temperature response (ΔTemp) normalised by total emissions rate change, due to removing SO_2 emissions from either the northern-hemisphere mid-latitudes (NHML), the US, Europe, East Asia, or India. The middle and right columns break this down into the global top-of-atmosphere effective radiative forcing (ERF) normalised by change in SO_2 emissions, and the global change in surface temperature normalised by global ERF (the climate sensitivity), the product of which gives the temperature response per unit emission change. Surface temperature changes are diagnosed from 150-year annual averages of coupled simulations, while ERF is diagnosed from 25-year annual averages of atmosphere-only simulations.

	$\Delta Temp / \Delta SO_2$ $(K\ (Tg\ yr^{-1})^{-1})$	$ERF / \Delta SO_2$ $(W\ m^{-2}\ (Tg\ yr^{-1})^{-1})$	$\Delta Temp / ERF$ $(K\ (Wm^{-2})^{-1})$
NHML	-0.0128 ± 0.0008	-0.0142 ± 0.0008	0.906 ± 0.077
US	-0.0164 ± 0.0037	-0.0163 ± 0.0037	1.00 ± 0.32
Europe	-0.0130 ± 0.0035	-0.0183 ± 0.0035	0.709 ± 0.231
East Asia	-0.0058 ± 0.0025	-0.0081 ± 0.0025	0.717 ± 0.385
India	-0.0109 ± 0.0095	-0.0184 ± 0.0095	0.594 ± 0.599

Table S2 | Clear-sky and all-sky shortwave (SW) and longwave (LW) effective radiative forcings (ERFs), due to removing SO_2 emissions from the northern hemisphere mid-latitudes (NHML), the US, Europe, East Asia, and India, in HadGEM3-GA4. In all cases, ERF is calculated as the annual mean difference in net down top-of-atmosphere flux between a 25-year atmosphere-only perturbation simulation and the control simulation. Total forcing is the sum of SW and LW components. Breaking down the ERF into clear-sky and all-sky, and shortwave and longwave components, we find that the longwave forcing in all cases is small, as would be expected given that sulfate interacts predominantly with shortwave solar radiation. As an interesting side note: the global mean change in clear-sky SW flux in the fully coupled simulations (not shown in table) turns out to be remarkably close to the all-sky SW forcing shown here (from the atmosphere-only simulations), for all the regions. Whether this is coincidence or not, we presently have no hypothesis.

		SW forcing ($W\ m^{-2}$)	LW forcing ($W\ m^{-2}$)	Total forcing ($W\ m^{-2}$)
Clear-sky	NHML	0.383 ± 0.043	-0.117 ± 0.049	0.266 ± 0.039
	US	0.079 ± 0.043	-0.020 ± 0.049	0.059 ± 0.039
	Europe	0.103 ± 0.043	0.013 ± 0.049	0.116 ± 0.039
	East Asia	0.104 ± 0.043	-0.059 ± 0.049	0.045 ± 0.039
	India	0.022 ± 0.043	0.009 ± 0.049	0.031 ± 0.039
All-sky	NHML	1.10 ± 0.049	-0.194 ± 0.064	0.906 ± 0.052
	US	0.276 ± 0.049	-0.044 ± 0.064	0.232 ± 0.052
	Europe	0.272 ± 0.049	0.003 ± 0.064	0.275 ± 0.052
	East Asia	0.240 ± 0.049	-0.075 ± 0.064	0.166 ± 0.052
	India	0.103 ± 0.049	-0.002 ± 0.064	0.101 ± 0.052

Table S3 | Surface temperature and precipitation responses separated by northern hemisphere (NH) and southern hemisphere (SH). Model grid-points lying exactly on the equator were included in the SH average.

		Δ Temperature (K)	Δ Precipitation (mm day^{-1})
NHML	**NH**	**1.18 ± 0.08**	**0.127 ± 0.0098**
	SH	*0.467 ± 0.044*	*-0.0006 ± 0.0083*
US	**NH**	**0.346 ± 0.078**	**0.0373 ± 0.0098**
	SH	*0.122 ± 0.044*	*-0.0022 ± 0.0083*
Europe	**NH**	**0.286 ± 0.078**	**0.0315 ± 0.0098**
	SH	*0.106 ± 0.044*	*0.0005 ± 0.0083*
East Asia	**NH**	**0.238 ± 0.078**	**0.0342 ± 0.0098**
	SH	*0.003 ± 0.044*	*-0.0177 ± 0.0083*
India	**NH**	**0.084 ± 0.078**	**0.0207 ± 0.0098**
	SH	*0.035 ± 0.044*	*-0.0122 ± 0.0083*

Table S4 | Percent variance explained by the three leading EOF modes of surface temperature (TS) and 500 hPa geopotential height (ϕ500) in the control simulation. Numbers in square brackets show the cumulative variance explained.

	TS variance explained (%)	φ500 variance explained (%)
EOF 1	20.5	22.3
EOF 2	10.1 [30.6]	11.8 [34.2]
EOF3	4.74 [35.3]	8.55 [42.7]